NUMERICAL ANALYSIS OF VISCOUS HYPERSONIC FLOW PAST A GENERIC FOREBODY

K.M. Wanie and M.A. Schmatz
Messerschmitt-Bölkow-Blohm GmbH
FE122, Postfach 80 11 60
D - 8000 München 80, FRG

Abstract

The viscous hypersonic flow past an analytically defined generic transport aircraft forebody is numerically simulated using a Navier-Stokes code. The governing equations are given in general three-dimensional curvilinear form and the computational method is outlined. The results are discussed in detail. Particular emphasis is layed upon the sensitivity of the solutions to variations of physical parameters. Main point of the investigation is the influence of turbulence, real gas effects and radiation on the global and local character of the flow. As it is expected turbulence has a significant influence on boundary-layer velocity profiles and boundary-layer thickness, while at the Mach number in consideration real gas effects and radiation play a minor role for these features. On the other hand it is found that real gas effects and radiation reduce the thermal loads considerably, resulting in less effort for isolation than indicated by predictions neglecting them.

1. Introduction

In the last few years a renewed interest in hypersonic flow problems could be observed. Large research programmes have been initiated for both reentry vehicles and hypersonic transport aircraft. While for the former a certain basis of experience is available from the US Space Shuttle [1], the opposite is true for hypersonic transport aircraft.

For hypersonic cruise flight aerodynamic drag and heating have to be minimized in order to save weight due to unnecessary fuel and isolation. In this context turbulence, location of the transition laminar-turbulent, real gas effects and radiation play a major role. Unfortunately rather poor experience is available today concerning the correct modelling of these physical parameters in hypersonic flow. Most of the turbulence models in use have been developed for incompressible or low Mach number flows. Although work is in progress to incorporate for example density gradients [2], a verification on a large scale is still lacking. Also in predicting transition laminar-turbulent work is in progress to determine for example the influence of nosetip bluntness or entropy layer swallowing for selected simple configurations [3, 4]. A general criterion, however, is not available. Furthermore it is not yet well explored which properties of the flow are influenced to what degree by real gas effects and radiation.

The present paper tries to alleviate the uncertainties mentioned to a certain extent by variation of the parameters in consideration within the possible range. In this way the sensitivity of the flow to these parameters can be estimated.

The investigations are done numerically by solution of the Navier-Stokes equations using the code NSFLEX [5]. In order to concentrate to the physical problems the calculations are restricted to a simple analytically given geometry which can be looked upon as the representation of a generic hypersonic cruise aircraft forebody. The three-dimensional problem is solved only for laminar flow to give a global image of the flow in consideration. For the subsequent parameter variations two-dimensional calculations are used in order to minimize the computational effort.

By means of the two-dimensional calculations the influence of turbulence, real gas effects and radiation on pressure, temperature and skin friction and on the development of the boundary-layer is investigated.

2. Governing equations

The general governing equations for the present investigations are the time dependent Reynolds-averaged compressible Navier-Stokes equations in conservation law form. In terms of body-fitted arbitrary coordinates ξ,η,ζ using Cartesian velocity components u,v,w they read

$$\mathbf{U}_t + \mathbf{E}_\xi + \mathbf{F}_\eta + \mathbf{G}_\zeta = \mathbf{0} \,, \qquad (1)$$

where

$$\mathbf{U}^T = J\,(\rho, \rho u, \rho v, \rho w, e)$$

is the solution vector of the conservative variables and

$$\mathbf{E} = J\,(\mathbf{E}\,\tilde{\xi}_x + \mathbf{F}\,\tilde{\xi}_y + \mathbf{G}\,\tilde{\xi}_z) \,, \qquad (2)$$

$$\mathbf{F} = J\,(\mathbf{E}\,\tilde{\eta}_x + \mathbf{F}\,\tilde{\eta}_y + \mathbf{G}\,\tilde{\eta}_z) \,,$$

$$\mathbf{G} = J\,(\mathbf{E}\,\tilde{\zeta}_x + \mathbf{F}\,\tilde{\zeta}_y + \mathbf{G}\,\tilde{\zeta}_z)$$

are the flux vectors normal to the ξ=const.,

η=const., ζ=const. faces. The Cartesian fluxes in Eq.(2) are

$$\tilde{E} = \begin{bmatrix} \rho u \\ \rho u^2-\sigma_{xx} \\ \rho uv-\sigma_{xy} \\ \rho uw-\sigma_{xz} \\ (e-\sigma_{xx})u-\sigma_{xy}v-\sigma_{xz}w+q_x \end{bmatrix} , \qquad (3)$$

$$\tilde{F} = \begin{bmatrix} \rho v \\ \rho vu-\sigma_{yx} \\ \rho v^2-\sigma_{yy} \\ \rho vw-\sigma_{yz} \\ (e-\sigma_{yy})v-\sigma_{yx}u-\sigma_{yz}w+q_y \end{bmatrix} ,$$

$$\tilde{G} = \begin{bmatrix} \rho w \\ \rho wu-\sigma_{zx} \\ \rho wv-\sigma_{zy} \\ \rho w^2-\sigma_{zz} \\ (e-\sigma_{zz})w-\sigma_{zx}u-\sigma_{zy}v+q_z \end{bmatrix}$$

with the stress tensor

$$\sigma_{xx} = -p - \frac{2}{3}\mu(-2u_x+v_y+w_z) , \qquad (4)$$

$$\sigma_{yy} = -p - \frac{2}{3}\mu(u_x-2v_y+w_z) ,$$

$$\sigma_{zz} = -p - \frac{2}{3}\mu(u_x+v_y-2w_z) ,$$

$$\sigma_{xy} = \sigma_{yx} = \mu(u_y+v_x) ,$$

$$\sigma_{xz} = \sigma_{zx} = \mu(w_x+u_z) ,$$

$$\sigma_{yz} = \sigma_{zy} = \mu(v_z+w_y)$$

and the heat flux vector

$$q_x = -k\,T_x , \qquad q_y = -k\,T_y , \qquad q_z = -k\,T_z . \qquad (5)$$

ρ,p,T,μ,k denote density, pressure, temperature, coefficient of viscosity and heat conductivity coefficient. The indices $()_\xi,()_\eta,()_\zeta,()_x,()_y,()_z$ denote partial derivatives with respect to ξ,η,ζ or x,y,z except for the stress tensor σ and the heat flux vector **q**.

The metric is defined by

$$\xi_x = (y_\eta z_\zeta - z_\eta y_\zeta)/J , \quad \xi_y = (x_\zeta z_\eta - x_\eta z_\zeta)/J ,$$

$$\xi_z = (x_\eta y_\zeta - x_\zeta y_\eta)/J ,$$

$$\eta_x = (z_\xi y_\zeta - y_\xi z_\zeta)/J , \quad \eta_y = (x_\xi z_\zeta - z_\xi x_\zeta)/J ,$$

$$\eta_z = (x_\zeta y_\xi - x_\xi y_\zeta)/J ,$$

$$\zeta_x = (y_\xi z_\eta - y_\eta z_\xi)/J , \quad \zeta_y = (x_\eta z_\xi - z_\eta x_\xi)/J ,$$

$$\zeta_z = (x_\xi y_\eta - x_\eta y_\xi , \qquad (6)$$

where

$$J = x_\xi(y_\eta z_\zeta - z_\eta y_\zeta) + y_\xi(x_\zeta z_\eta - x_\eta z_\zeta) + z_\xi(x_\eta y_\zeta - x_\zeta y_\eta) \qquad (7)$$

is the cell volume.

To simulate turbulent flows effective transport coefficients are introduced with the Boussinesq approximation. The equations are closed with an algebraic turbulence model.

3. Numerical method

To reach the steady state solution asymptotically the governing equations are solved in time-dependent form by the finite-volume method NSFLEX [5, 6, 7]. In order to allow for high CFL numbers point Gauss-Seidel relaxation is applied to the unfactored implicit equations.

Time integration.

With the first order in time discretized implicit form of Eq. (1),

$$(\mathbf{U}^{n+1} - \mathbf{U}^n)/\Delta t + \mathbf{E}_\xi^{n+1} + \mathbf{F}_\eta^{n+1} + \mathbf{G}_\zeta^{n+1} = \mathbf{0}, \qquad (8)$$

a Newton method can be constructed for $\mathbf{U}^{n+1}$. For this purpose the fluxes of Eq. (8) are linearized about the known time level n,

$$\mathbf{E}^{n+1} = \mathbf{E}^n + \mathbf{A}^n\Delta\mathbf{U} , \quad \mathbf{F}^{n+1} = \mathbf{F}^n + \mathbf{B}^n\Delta\mathbf{U} , \qquad (9)$$

$$\mathbf{G}^{n+1} = \mathbf{G}^n + \mathbf{C}^n\Delta\mathbf{U} ,$$

leading to

$$\Delta\mathbf{U}/\Delta t + (\mathbf{A}^n\Delta\mathbf{U})_\xi + (\mathbf{B}^n\Delta\mathbf{U})_\eta + (\mathbf{C}^n\Delta\mathbf{U})_\zeta = \qquad (10)$$

$$-(\mathbf{E}_\xi + \mathbf{F}_\eta + \mathbf{G}_\zeta)^n = \mathrm{RHS} .$$

The Jacobians **A**, **B**, **C** of the flux vectors **E**, **F**, **G** are defined by

$$\mathbf{A} = \partial\mathbf{E}/\partial\mathbf{U} , \quad \mathbf{B} = \partial\mathbf{F}/\partial\mathbf{U} , \quad \mathbf{C} = \partial\mathbf{G}/\partial\mathbf{U} . \qquad (11)$$

$\Delta\mathbf{U}$ is the time variation of the solution and therefore the update is

$$\mathbf{U}^{n+1} = \mathbf{U}^n + \Delta\mathbf{U} . \qquad (12)$$

With the divergence of the fluxes on the right-hand side (RHS), Eq. (10) has to be solved approximately at every time step. A point Gauss-Seidel technique is used, where it is not necessary to balance the equation perfectly. The terms $(\mathbf{A}^n\Delta\mathbf{U})_\xi$, $(\mathbf{B}^n\Delta\mathbf{U})_\eta$, $(\mathbf{C}^n\Delta\mathbf{U})_\zeta$ on the LHS are discretized at i,j,k up to second order in space [5]. For example $(\mathbf{A}^n\Delta\mathbf{U})_\xi$ is discretized along j,k=const by

$$(\mathbf{A}^n\Delta\mathbf{U})_\xi = (\mathbf{A}_{inv}{}^n\Delta\mathbf{U})_{i+1/2} - (\mathbf{A}_{inv}{}^n\Delta\mathbf{U})_{i-1/2} + (\mathbf{A}_{vis}{}^n)_i(\Delta\mathbf{U}_{i+1} - 2\Delta\mathbf{U}_i + \Delta\mathbf{U}_{i-1}) , \qquad (13)$$

where

$$(\mathbf{A}_{inv}{}^n\Delta\mathbf{U})_{i+1/2} = (\mathbf{T}\Lambda^+\mathbf{T}^{-1})_{i+1/2}\Delta\mathbf{U}^+_{i+1/2} + (\mathbf{T}\Lambda^-\mathbf{T}^{-1})_{i+1/2}\Delta\mathbf{U}^-_{i+1/2} ,$$

$$(\mathbf{A}_{inv}{}^n\Delta\mathbf{U})_{i-1/2} = (\mathbf{T}\Lambda^+\mathbf{T}^{-1})_{i-1/2}\Delta\mathbf{U}^+_{i-1/2} + (\mathbf{T}\Lambda^-\mathbf{T}^{-1})_{i-1/2}\Delta\mathbf{U}^-_{i-1/2} . \qquad (14)$$

$\Delta\mathbf{U}$ vectors are extrapolated consistently to the right-hand side up to second order. $\mathbf{A}_{vis}$ is the thin-layer viscous Jacobian at i,j,k for all directions ξ,η,ζ. Λ is the diagonal matrix of the

eigenvalues of the Jacobian **A**. **T** and $\mathbf{T}^{-1}$ are the matrices which diagonalize **A** ($\Lambda = \mathbf{T}^{-1}\mathbf{A}\mathbf{T}$). The coefficients of **T**, Λ, $\mathbf{T}^{-1}$ are found from arithmetic means of the conservative variables ρ, ρu, ρv, ρw, e. Λ^+ is the diagonal matrix of the positive eigenvalues of $\mathbf{A}_{inv}$ and Λ^- the matrix of the negative ones,

$$\Lambda^+ = \max(E,\Lambda) , \qquad \Lambda^- = \min(-E,\Lambda) . \tag{15}$$

The term

$$E = \beta * SMREL * \max(\mathrm{abs}(\lambda_4),\mathrm{abs}(\lambda_5)) \tag{16}$$

is zero where β is zero and leads to an additional residual smoother at non-monotonous flow regions. β is zero for smooth flow situations and one for non-monotonous ones. SMREL is typically set to 0.3. With these discretisation formulas applied to the three spatial directions, the equation is reordered for point Gauss-Seidel iteration,

$$\mathbf{DIAG}_{i,j,k}{}^{n}\,\Delta\mathbf{U}_{i,j,k}{}^{\mu+1} = -\mathbf{RHS}_{i,j,k}{}^{n} + \mathbf{ODIAG}_{i,j,k} . \tag{17}$$

The iteration count is indicated by an upper index μ. $\mathbf{DIAG}_{i,j,k}{}^{n}$ is a 5*5 matrix of the sum of the eigenvalue splitted inviscid and the viscous thin-layer Jacobians together with the inverse of the time step $1/\Delta t$. The time step is calculated with the maximum of the eigenvalues of the inviscid Jacobians,

$$\Delta t = (\beta * CFLMIN + (1.-\beta) * CFL)/(\max|\lambda_{i,j,k}|) . \tag{18}$$

The CFL number is typically about 150 to 200 for moderate Mach numbers and may reduce to lower ones for hypersonic applications in the transient phase. CFLMIN limits the time step at regions where strong shocks appear and may need to be set to about 10 for high Mach numbers. The fluxes $\mathbf{RHS}_{i,j,k}{}^{n}$ and the matrix $\mathbf{DIAG}_{i,j,k}{}^{n}$ rest at time level n during μ-iteration. The term **ODIAG** is given by

$$\begin{aligned}\mathbf{ODIAG} = f(&\Delta\mathbf{U}_{i+1,j,k},\Delta\mathbf{U}_{i-1,j,k},\Delta\mathbf{U}_{i,j+1,k},\\ &\Delta\mathbf{U}_{i,j-1,k},\Delta\mathbf{U}_{i,j,k+1},\Delta\mathbf{U}_{i,j,k-1}),\end{aligned} \tag{19}$$

where the actual $\Delta\mathbf{U}$ values of the μ-iteration are taken. Three Gauss-Seidel steps (μ=1(1)3) are typically performed at every time step.

Two features of the scheme are important to allow high CFL numbers:

- True Jacobians of the fluxes on the RHS must be used on the LHS.

- In [5, 8] it was found that for high Mach numbers and/or for high cell aspect ratios the matrix $\mathbf{DIAG}_{i,j,k}$ may have zero or even negative diagonal elements, a fact which was observed by other authors, too [9, 10]. Here a pre-conditioning of the matrix $\mathbf{DIAG}_{i,j,k}$ is done such that diagonal dominance is forced [5, 8]. The system is solved for the non-conservative $\Delta\mathbf{U}^*$ vector by Gauss elimination and transformed back to a conservative $\Delta\mathbf{U}$ at every point i,j,k ,

$$\begin{aligned}&(\mathbf{DIAG}_{i,j,k}{}^{n})^* \ (\Delta\mathbf{U}_{i,j,k}{}^{\mu+1})^* = -\ \mathbf{RHS}_{i,j,k}{}^{n} + \mathbf{ODIAG}_{i,j,k} ,\\ &\Delta\mathbf{U}_{i,j,k}{}^{\mu+1} = \mathbf{M}\ (\Delta\mathbf{U}_{i,j,k}{}^{\mu+1})^*\end{aligned} \tag{20}$$

with

$$(\mathbf{DIAG}_{i,j,k}{}^{n})^* = \mathbf{DIAG}_{i,j,k}{}^{n}\ \mathbf{M} .$$

M is the matrix to transform **U** to non-conservative variables $\mathbf{U}^*=(\rho,u,v,w,p)^T$

$$\mathbf{M}=\partial\mathbf{U}/\partial\mathbf{U}^* .$$

This transformation does not at all influence the conservation properties of the scheme [5, 8].

Flux calculation.

Inviscid fluxes. For the inviscid flux calculation a linear locally one-dimensional Riemann solver for **E,F,G** is employed at each finite-volume face. A hybrid local characteristic (LC) [11] and Steger-Warming type (SW) scheme is employed, which allows the code to work for a wide range of Mach numbers (.05 < Mach < 100), see also [12]. For example, the flux at cell face i+1/2 is found by

$$\mathbf{E}_{i+1/2} = (\mathbf{E}_{LC}(1-a) + a*\mathbf{E}_{SW})_{i+1/2} \tag{21}$$

with $a=SW*s*(M_r-M_l)^2$. s is the van Albada sensor [13] for the density, M_r and M_l are the Mach numbers on the left- and on the right-hand side of the volume face. SW is an input constant to be specified greater or equal to zero. To calculate the local characteristic fluxes, the conservative variables on either side of the volume face are extrapolated up to third order in space (MUSCL type extrapolation) by

$$\begin{aligned}\mathbf{U}_l &= \mathbf{U}_i + s/4*((1-k*s)\Delta_- + (1+k*s)\Delta_+)_i ,\\ \mathbf{U}_r &= \mathbf{U}_{i+1} - s/4*((1-k*s)\Delta_+ + (1+k*s)\Delta_-)_{i+1} ,\end{aligned} \tag{22}$$

where k=1/3 for third order upwind biased extrapolation. The index l means state to the left and the index r state to the right. s is a van Albada type sensor [13]

$$\begin{aligned}&s=(2\Delta_+\Delta_- + \varepsilon)/((\Delta_+)^2 + (\Delta_-)^2 + \varepsilon)\\ &\text{with } \Delta_+=\mathbf{U}_{i+1}-\mathbf{U}_i , \quad \Delta_-=\mathbf{U}_i-\mathbf{U}_{i-1} .\end{aligned} \tag{23}$$

ε is the vector

$$\varepsilon = \varepsilon' * \max(ZERO, \mathbf{U}_l{}^{**}2, \mathbf{U}_r{}^{**}2). \tag{24}$$

ε' controls the sensor and is typically set to ε'=5.E-5. The number ZERO is a constant in the code to avoid division by 0.0 wherever needed (ZERO=1.E-20). The number β for use on the left-hand side is $\beta=\max(a,s)$ (a from Eq. (21) and s is the maximum from Eq. (23)). With the variables $\mathbf{U}_l$ and $\mathbf{U}_r$ an eigenvalue weighted mean value is found at the volume face by

$$\mathbf{U}_{i+1/2} = \mathbf{T}_{i+1/2} * (\ \Lambda'^{+}\mathbf{T}^{-}{}_{i+1/2}\mathbf{U}_l + \Lambda'^{-}\mathbf{T}^{-}{}_{i+1/2}\mathbf{U}_r\ ), \tag{25}$$

where the matrixes Λ'^{+}, Λ'^{-} are diagonal matrixes,

$$\begin{aligned}\lambda'_i{}^{+} &= .5*(1+(\lambda_{i_l}+\lambda_{i_r})/(ZERO+\mathrm{abs}(\lambda_{i_l})+\mathrm{abs}(\lambda_{i_r}))) ,\\ \lambda'_i{}^{-} &= .5*(1-(\lambda_{i_l}+\lambda_{i_r})/(ZERO+\mathrm{abs}(\lambda_{i_l})+\mathrm{abs}(\lambda_{i_r}))) .\end{aligned} \tag{26}$$

The index i here denotes the i-th eigenvalue (i=1(1)5). With the backward Riemann solution $\mathbf{U}_{i+1/2}$ the inviscid fluxes can be calculated directly (flux difference splitting),

$$\mathbf{E}_{LC} = \mathbf{E}(\mathbf{U}_{i+1/2}) . \tag{27}$$

This scheme guarantees the homogeneous property of the Euler fluxes, a property which simplifies the evaluation of the true Jacobians of the fluxes for use on the left-hand side [5, 8].

Because this local characteristic flux is not diffusive enough to guarantee stability for hypersonic flow cases especially in the transient phase, where shocks move, at regions of high gradients a new **hyper-diffusive flux** is used locally. It is a modified Steger-Warming [14] type flux (flux vector splitting),

$$E_{SWi+1/2} = E_i^+ + E_{i+1}^- = (T\Lambda^+ T^- U)_i + (T\Lambda^- T^- U)_{i+1} \quad . \quad (28)$$

The modifications of the original Steger-Warming fluxes are [15]

$$\lambda_{1,2,3}^+ = 0.5*(\lambda_3^+ + \lambda_4^+) \quad , \quad (29)$$
$$\lambda_{1,2,3}^- = 0.5*(\lambda_3^- + \lambda_4^-) \quad ,$$
$$\text{Energy flux} = \text{mass flux} * H_{tot} \quad , \quad (30)$$

where H_{tot} is the total enthalpy of the corresponding cell. Eq. (30) gives a better conservation of the total enthalpy as was also found in [9] for the van Leer flux vector splitting scheme. Eq. (29) avoids the unsteadyness of the mass flux in the original Steger-Warming flux.

Diffusive fluxes. Diffusive fluxes at the cell faces are calculated with central differences, for example, at a ξ=const. cell face

$$\phi = \phi_{i+1,j,k} - \phi_{i,j,k} \quad . \quad (31)$$

ϕ represents the velocity components u,v,w or the temperature T. For the cross derivatives, where ϕ_η and ϕ_ζ are needed, conventional differencing is used:

$$\phi_\eta = (\phi_{i+1/2,j+1,k} - \phi_{i+1/2,j-1,k})/2 \quad , \quad (32)$$
$$\phi_\zeta = (\phi_{i+1/2,j,k+1} - \phi_{i+1/2,j,k-1})/2 \quad ,$$

where the ϕ-values are found as arithmetic means of the neighbouring cell center values.

Boundary conditions.
At the outer farfield boundaries non-reflecting boundary conditions are inherent in the code since at every cell face a Riemann problem is solved and therefore the code extracts only such information from the boundary which is allowed by the characteristic theory. At outflow boundaries, as long as the flow is supersonic, the code does not need information from downstream. In the part of the viscous regime where the flow is subsonic the solution vector is extrapolated constantly. No upstream effect of this extrapolation could be observed as long as the flow streams downstream.

At solid bodies the no-slip condition

$$u = v = w = 0 \quad . \quad (33)$$

holds.

The following temperature and heat flux boundary conditions are possible to prescribe:

- adiabtic wall: $q_w = 0$, (34a)
- given heat flux : q_w , (34b)
- given temperature : T_w . (34c)

Radiation of solid bodies can also be taken into account. In this case the heatflux vector at the wall, here written for simplicity in Cartesian coordinates, is calculated with

$$q = - kT_z + \varepsilon\sigma T_w^4 \quad . \quad (35)$$

The second term in Eq. (35) is the radiation term. σ is the Stephan-Boltzmann constant with $\sigma=5.67*10^{-8}$ $W/(m^2K^4)$. ε is the emissivity factor ($0\leq\varepsilon\leq1$). T_w is the temperature at the wall. For a systematic study on the Reynols-number effect on flow simulations with radiation boundary conditions see [16].

Equilibrium real gas incorporation.
At first the influence of the real gas behaviour on the inviscid fluxes is described. In the Euler equations the ratio of the specific heats appears only in the energy equation, written here for simplicity in cartesian coordinates,

$$(e_r)_t + (u(p+e_r))_x + (v(p+e_r))_y + (w(p+e_r))_z = 0 \quad (36)$$

with

$$e_r = p/(\gamma_r-1) + \rho q^2/2 \quad , \quad \gamma_r = \gamma_r(p,\rho) \quad . \quad (37)$$

The index r denotes real equilibrium gas. $\gamma_r = \gamma_r(p,\rho)$ is calculated from a thermodynamic subroutine. Following EBERLE [12] we define a new total energy e with a reference ratio of specific heats γ which is the free stream γ

$$e = p/(\gamma-1) + \rho q^2/2 \quad . \quad (38)$$

With

$$e_r = e + Q \quad , \quad (39)$$
$$Q = e_r - e = p(1/(\gamma_r-1)-1/(\gamma-1))$$

the energy equation is now

$$(e)_t + (Q)_t + (u(p+e))_x + (v(p+e))_y + (w(p+e))_z = -((u*Q)_x + (v*Q)_y + (w*Q)_z) \quad . \quad (40)$$

We are just interested in the steady state solution and therefore we can use a steadiness assumption for the source term Q,

$$(Q)_t = 0 \quad . \quad (41)$$

This means that the left-hand side of Eq. (40) is the perfect gas energy equation and the real gas influence is separated on the right-hand side as a source term. This pseudo-unsteady approach now offers the big advantage that neither the Riemann solver nor the implicit part of the NSFLEX solver has to be changed. Also the static pressure can be calculated as usual directly from the flow variables with $p=(\gamma-1)*(e-.5*\rho q^2)$. Note that γ is the free stream ratio of specific heats and that in the code only a few lines are necessary to calculate the source terms. This approach is restricted to steady flow simulations.

To account for the effects of deviation from perfect gas assumption in the viscous fluxes some more thermodynamic subroutines for the temperature and the transport coefficients have to be used,

$$T = T(p,\rho) \quad , \quad \mu = \mu(p,\rho) \quad , \quad k = k(p,\rho) \quad . \quad (42)$$

New vectorized spline representations of the thermodynamic equilibrium properties [17, 18] are used, such that a real gas calculation costs only about eight percent more than a perfect gas calculation.

4. Results

Since for the present investigations the physical problems are of primary interest, a simple generic geometry was analytically defined for the calculations to represent a hypersonic transport aircraft forebody. A three-dimensional laminar calculation was performed to get a general image of the flow in considertion. The influence of the parameters mentioned in Chapter 1 was subsequently studied by means of two-dimensional calculations in order to minimize the computational effort.

The surface of the body is defined by

$$\frac{y^2}{a^2} + \frac{z^2}{b^2} = 1 , \qquad (42)$$

where

$$a = -0.0533\sqrt{x} - 0.0912\,x - 0.1790\,x^2 + 0.1990\,x^3 - 0.0632\,x4 , \quad (43a)$$

$$b = -0.0271\sqrt{x} - 0.0110\,x - 0.1270\,x^2 + 0.1730\,x^3 - 0.0640\,x4 . \quad (43b)$$

This geometry is characterized by a blunt nose and elliptical cross sections. It is symmetrical with respect to the planes y=0 and z=0. The nosetip bluntness is relatively small compared to the total body length and the metric of the surface is very smooth.

The grid used for the three-dimensional calculations is shown in Fig. 1. Depicted are the surface grid, the plane of symmetry and an i=const cut. The grid contains 75 cells in streamwise, 70 cells in circumferential and 64 cells in wall normal direction, respectively. The i=const. lines of the surface grid are situated in x=const. cuts, the x-stations being defined by a simple cubic function. The circumferential point distribution is characterized by a constant increment of the angle between the centerline and two points (i,j) and (i,j+1). Particular emphasis was layed upon a proper resolution of the blunt nosetip.

The space grid was generated in two steps. First an inner wall-normal mesh was obtained from simple algebraic relations. This mesh extends to about about 10 percent of the distance between the wall and the outer boundary, which was adapted to the flow conditions by estimation of the shock position. The outer region was then covered with points by solving a system of elliptic differential equations [19], using the wall-normal mesh as boundary condition. For the two-dimensional calculations a cut of the three-dimensional grid at y=0 was used.

On the grid described a laminar three-dimensional calculation was performed. The flow was characterized by free stream Mach number M_∞=6.8, Reynolds number referenced to the total body length Re=122 000 000, angle of attack α=6°, free stream temperature T_∞=227K and adiabatic wall.

The isobars and Mach-isolines for this calculation are presented in Fig. 2 and 3, respectively. The pressure distribution is quite smooth along the surface, steep gradients exist only in the nose region. Note that the spatial representation of the bow shock could be improved significantly by a better adaption of the grid in the shock region. It was found, however, that this has almost no influence on the results near the body surface, which are of primary interest here. Fig. 4 shows the isotherms calculated.

In Fig. 5 isobars are given for the laminar two-dimensional calculation. Note that in Fig. 2 and 5 the same levels were used for the isolines in order to allow a comparison. As expected, the shock is further away from the body and the pressure along the body is higher for the two-dimensional case.

In Figs. 6 to 10 two-dimensional computations for

- laminar flow, perfect gas,
- turbulent flow, perfect gas,
- turbulent flow, real gas,
- turbulent flow, real gas, radiation,

are compared. For all turbulent cases transition was fixed at 10 per cent of the body length. For case 4 the emissivity factor in the radiation boundary condition was set to ε=0.85.

In Fig. 6 the computed c_p-distributions along the upper and lower surface are given for the four test cases. As it is expected only little differences are discernable.

Fig. 7 shows the tangential velocity components at various stations along the lower side of the body. While the profiles are almost identical at a station upstream of transition laminar-turbulent (Fig.7a), the usual significant differences are found between the laminar profile and the turbulent ones in the turbulent flow (Fig. 7b,c). No evident influence of real gas effects or radiation on the turbulent velocity profiles gets obvious from Fig. 7. As a consequence from this it can be stated that real gas effects and radiation do not significantly influence the boundary-layer thickness for the present case. Note that for Fig. 7 the profiles have not been normalized with respect to the boundary-layer thickness.

Fig. 8 gives the temperature distributions along the lower and upper side for the four test cases. Compared to the laminar flow the turbulent case without real gas and radiation yields somewhat higher temperatures. If real gas effects are included a significant reduction of the overall wall temperature can be found. The application of radiation boundary conditions finally reduces the temperatures again considerably. Note that the indentations at x=0.1 in the temperature distributions of the turbulent cases are due to the fact that no transitional region is modelled. The turbulent viscosity is switched on there abruptly.

When comparing the temperature profiles along the lower side (Fig. 9) the expected differences are found between laminar and turbulent flow, that is the temperature gradients near the wall are much steeper for the turbulent cases (Fig. 9b,c). The influence of real gas and radiation is confined to the immediate neighbourhood of the wall.

Finally the distribution of the skin friction coefficient c_f (Fig. 10) shows the usual behaviour for laminar and turbulent flow. The location of the transition at x_{tr}=0.1 is clearly discernable. Compared to the differences between turbulent and laminar flow the variation within the turbulent results is relatively small.

5. Conclusions

A Navier-Stokes code was used to simulate the hypersonic flow past an analytically given generic forebody of a hypersonic transport aircraft. The governing equations were given in general coordinates and the numerical method was described. Results were presented and compared for laminar and turbulent flow. For the turbulent case both perfect gas and equilibrium real gas assumption with radiation boundary condition were used optionally.

The pressure distribution was found to be relatively insensitive to changes in the above conditions. The development of the boundary-layer velocity profiles and the boundary-layer thickness are influenced, of course, by the location of the transition laminar-turbulent but are relatively insensitive to the choice of perfect or real gas assumption and radiation. The opposite was found for the surface temperature distribution, where considerable reductions of the thermal loads were found using real gas assumption and radiation boundary conditions.

Presently work is under progress to incorporate nonequilibrium real gas assumptions into the code. Furthermore due to the multitude of parameter variations and sensitivity studies necessary to obtain insight in the behaviour of flow at hypersonic speed it turned out to be imperative to reduce the computational effort as far as possible. Therefore a space marching option is introduced currently into the NSFLEX code using line relaxation and bow shock fitting. In this modified code block- or plane-marching will be available using the parabolized Navier-Stokes equations whereever possible.

In addition the experience gained from the development of the zonal solution technique [20, 21] will be implemented to a coupled Euler/second-order boundary-layer code [5]/[22] designed especially for hypersonic flow problems. The comparison of the different types of modelling flow should help to verify the numerical results.

Acknowledgement: The authors want to thank the IABG-Ottobrunn VP200 supercomputer group for their support.

6. References

[1] Arrington, J.P., Jones, J.J. (eds.): Shuttle performance: Lessons learned, NASA CP 2283, 1983.

[2] Situ, M., Schetz, J.: New mixing lenght model for turbulent high speed flow. AIAA-Paper 89-1821, 1989.

[3] Stetson, K.F., Thompson, E.R., Donaldson, J.C, Siler, L.G..: Laminar boundary layer stability experiments on cone at Mach 8, part 2: blunt cone. AIAA-Paper 84-0006, 1984.

[4] Malik, M.R., Spall, R.E., Chang, C.-L.: Effect of nose bluntness on boundary layer stability and transition. AIAA-Paper 90-0112, 1990.

[5] Schmatz, M.A.: Three-dimensional viscous flow simulations using an implicit relaxation scheme. Kordulla, W. (ed.): Numerical simulation of compressible viscous-flow aerodynamics, Notes on Numerical Fluid Mechanics (NNFM), Vol. 22, Vieweg, Braunschweig, 1988, pp. 226-242.

[6] Schmatz, M.A., Brenneis, A., Eberle, A.: Verification of an implicit relaxation method for steady and unsteady viscous and inviscid flow problems. AGARD CP 437, 1988, pp. 15-1 - 15-33.

[7] Schmatz, M.A.: Hypersonic three-dimensional Navier-Stokes calculations for equilibrium gas. AIAA-paper 89-2183, 1989.

[8] Eberle, A., Schmatz, M.A., Schäfer, O.: High-order solutions of the Euler equations by characteristic flux averaging. ICAS-paper 86-1.3.1, 1986.

[9] Hänel, D., Schwane, R.: An implicit flux-vector splitting scheme for the computation of viscous hypersonic flow. AIAA-paper 89-0274, 1989.

[10] Thomson, D., Matus, R.: Conservation errors and convergence characteristics of iterative space-marching algorithms. AIAA-paper, 89-1935, 1989.

[11] Eberle, A.: 3D Euler calculations using characteristic flux extrapolation. AIAA-paper 85-0119, 1985.

[12] Eberle, A.: Characteristic flux averaging approach to the solution of Euler's equations. VKI lecture series, Computational fluid dynamics, 1987-04, 1987.

[13] Anderson, W.K., Thomas, J.L., van Leer, B.: A comparison of finite volume flux vector splittings for the Euler equations. AIAA-paper 85-0122, 1985.

[14] Steger, J.L., Warming, R.F.: Flux vector splitting of the inviscid gasdynamic equations with application to finite difference methods. J. Comp. Phys., Vol. 40, 1981, pp. 263-293.

[15] Schmatz, M.A.: NSFLEX - An implicit relaxation method for the Navier-Stokes equations for a wide range of Mach numbers. Proc. 5th GAMM-Seminar, NNFM 30, Vieweg, Braunschweig, 1990.

[16] Hirschel, E.H., Mundt, C., Monnoyer, F., Schmatz, M.A.: Reynolds-number dependency of radiation-adiabatic wall temperature. In preparation, 1990.

[17] Fischer, J.: Entwicklung verbesserter Approximationen der Zustandsfunktionen für atmosphärische Luft im thermo-chemischen Gleichgewicht. Diploma Thesis, Techn. University Munich, 1989.

[18] Mundt, Ch., Keraus, R., Fischer, J.: Improved real gas curve fits for air at thermo-chemical equilibrium. To appear in ZFW, 1990.

[19] Schwarz, W.: Elliptic grid generation system for three-dimensional configurations using Poisson's equation. In: Häuser, J., Taylor, C. (eds.): Proc. 1st int. conf. on num. grid generation in comp. fluid dynamics. Pineridge Press, 1986, pp. 341-352.

[20] Wanie, K.M.; Schmatz, M.A.; Monnoyer, F.: A close coupling procedure for zonal solutions of the Navier-Stokes, Euler and boundary-layer equations. ZFW, Vol. 11, 1987, pp. 347-359.

[21] Schmatz, M.A., Monnoyer, F., Wanie, K.M., Hirschel, E.H.: Zonal solutions of three-dimensional viscous flow problems. In: Zierep, J., Oertel, H. (eds.): Symposium Transsonicum III. Springer, 1988.

[22] Monnoyer, F.: Calculation of three-dimensional attached viscous flow on general configurations with second-order boundary-layer theory. ZFW, Vol. 14, 1990, pp. 95-108.

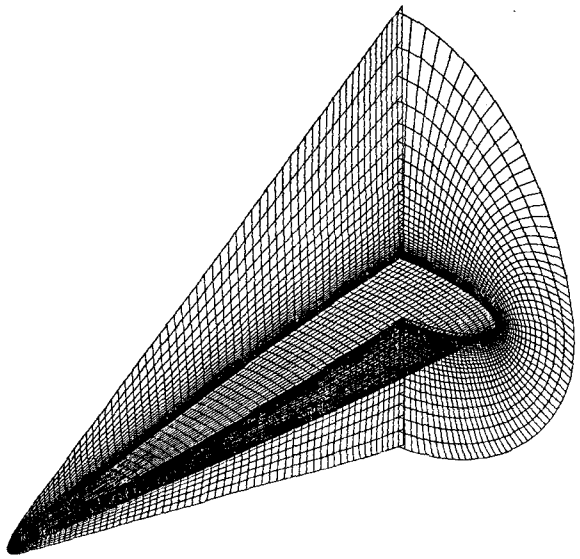

Fig. 1 Computational grid for generic hypersonic forebody (75*70*64 cells)

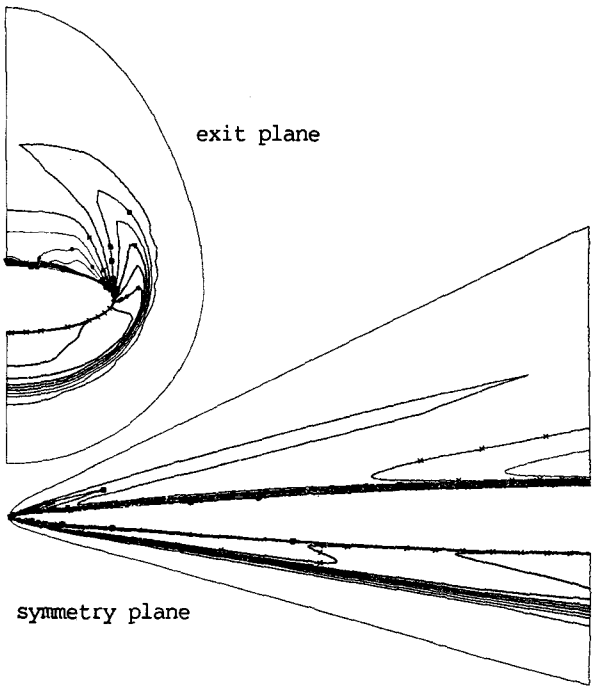

Fig. 3 Mach contours, generic forebody (M_∞=6.8, α=6°, Re=122 000 000, T_∞=227.65 K, laminar)

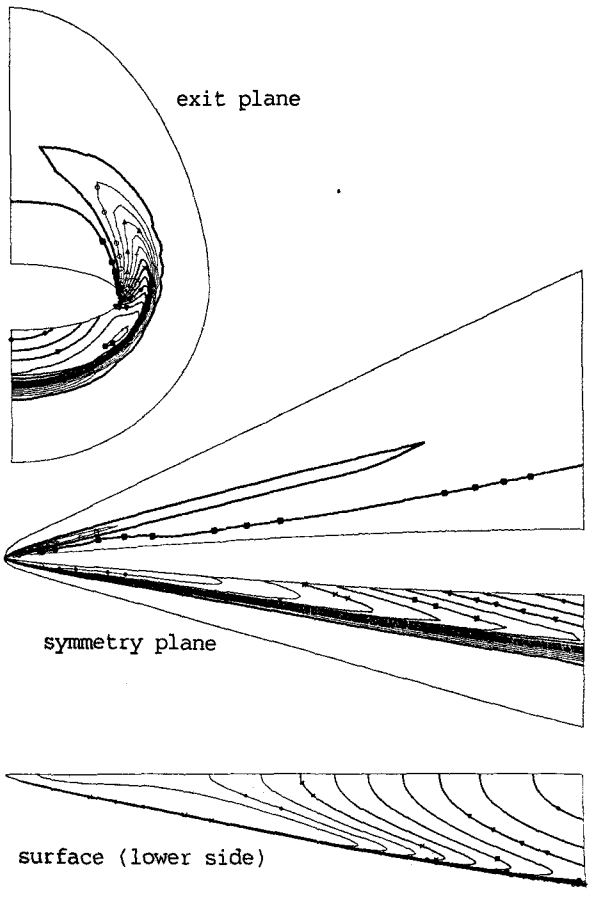

Fig. 2 Isobars, generic forebody (M_∞=6.8, α=6°, Re=122 000 000, T_∞=227.65 K, laminar)

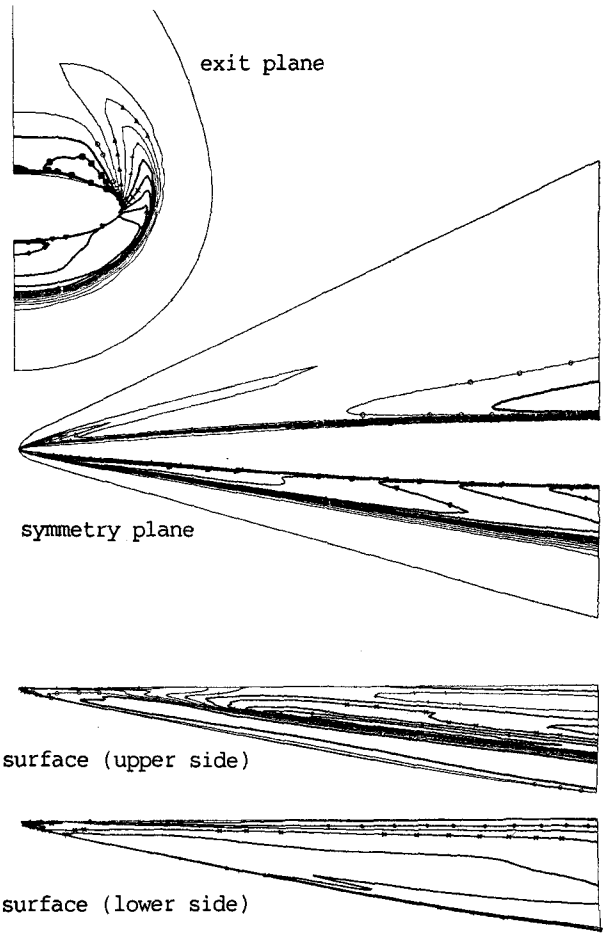

Fig. 4 Isotherms, generic forebody (M_∞=6.8, α=6°, Re=122 000 000, T_∞=227.65 K, laminar)

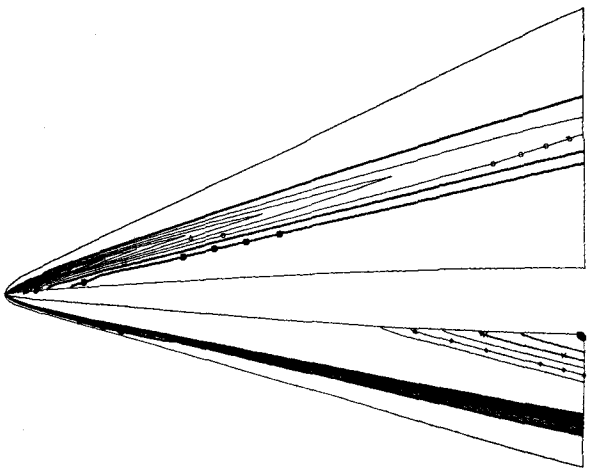

Fig. 5 Isobars, generic forebody (2D, M_∞=6.8, α=6°, Re=122 000 000, T_∞=227.65 K, laminar)

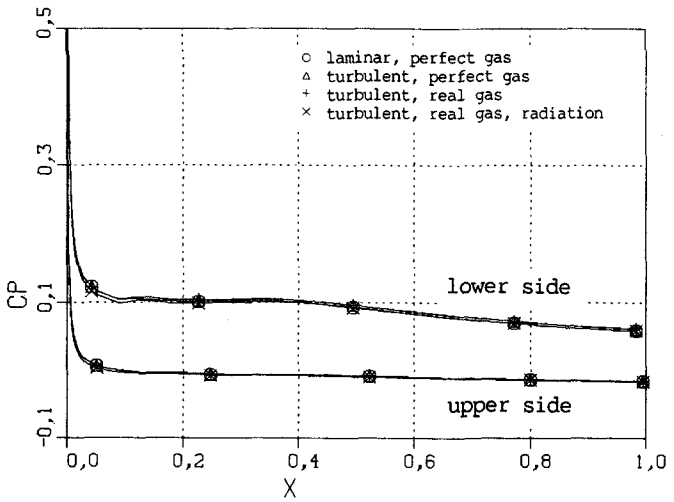

Fig. 6 c_p-distributions for perfect and real gas calculations, generic forebody (2D, M_∞=6.8, α=6°, Re=122 000 000, T_∞=227.65 K)

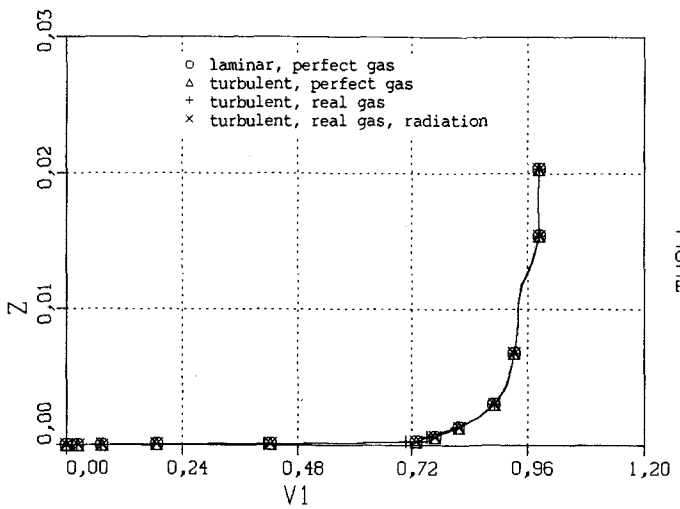

7a) x = 0.05

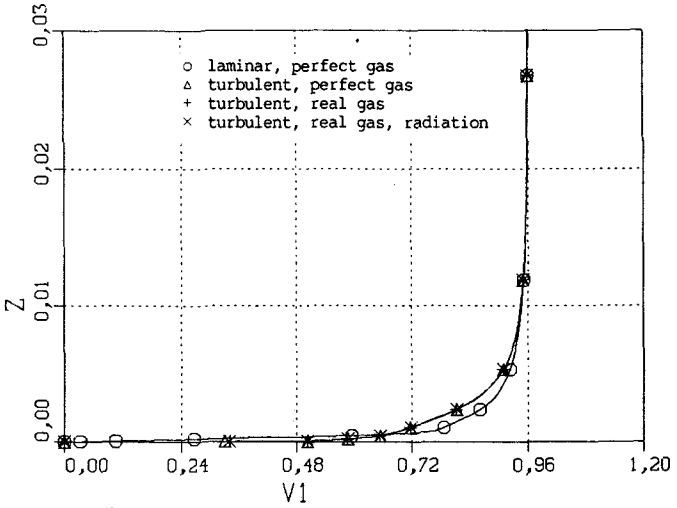

7b) x = 0.35

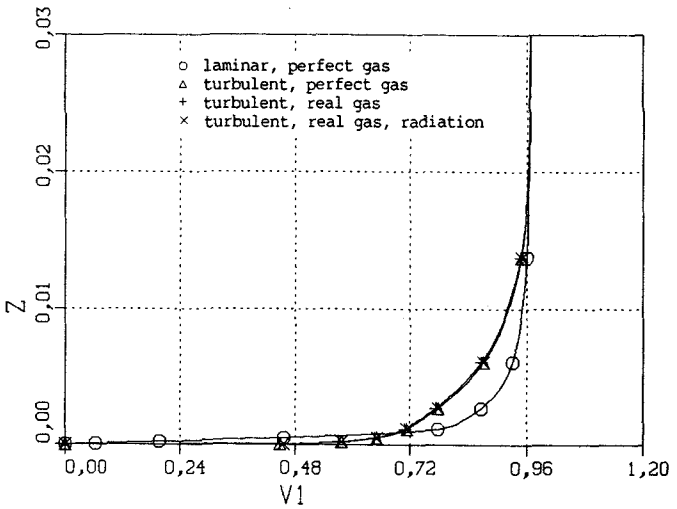

7c) x = 0.90

Fig. 7 Tangential velocity profiles for perfect and real gas calculations, generic forebody (2D, M_∞=6.8, α=6°, Re=122 000 000, T_∞=227.65 K)

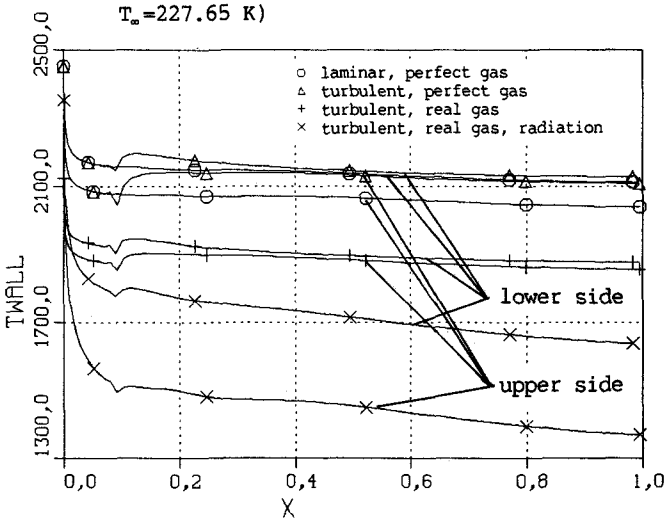

Fig. 8 Temperature distributions for perfect and real gas calculations, generic forebody (2D, M_∞=6.8, α=6°, Re=122 000 000, T_∞=227.65 K)

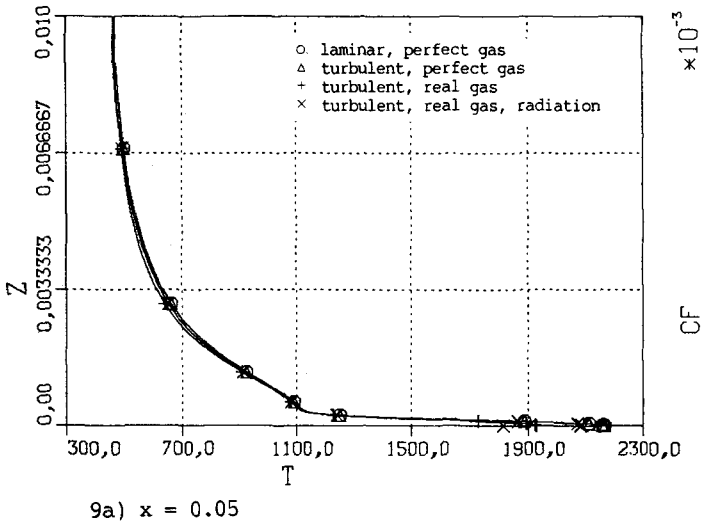

9a) x = 0.05

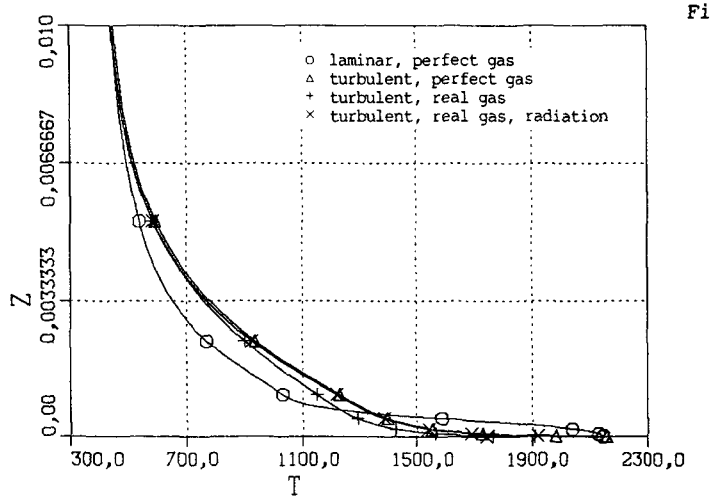

9b) x = 0.35

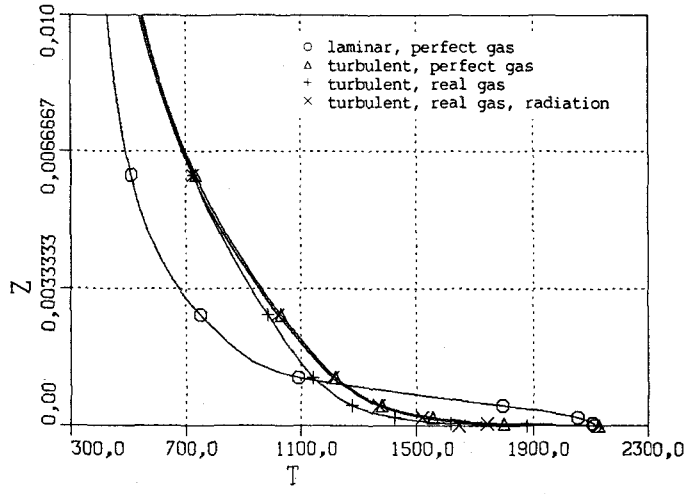

9c) x = 0.90

Fig. 9 Temperature profiles for perfect and real gas calculations, generic forebody (2D, M_∞=6.8, α=6°, Re=122 000 000, T_∞=227.65 K)

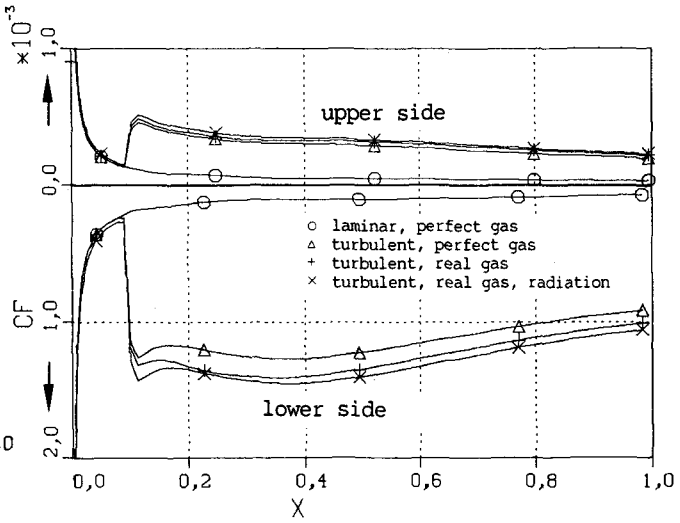

Fig. 10 c_f-distributions for perfect and real gas calculations, generic forebody (2D, M_∞=6.8, α=6°, Re=122 000 000, T_∞=227.65 K)